

Refined Setup for Angle-Resolved Photoluminescence Spectroscopy of Thin Films

Christian Hänisch¹, Simone Lenk, and Sebastian Reineke^{1*}

Dresden Integrated Center for Applied Physics and Photonic Materials (IAPP) and Institute for Applied Physics, Technische Universität Dresden, Nöthnitzer Strasse 61, Dresden 01187, Germany

 (Received 16 September 2019; revised 9 March 2020; accepted 30 October 2020; published 10 December 2020)

Angle-resolved photoluminescence spectroscopy is a powerful tool for investigation of the properties of light-emitting thin-film structures. For instance, it can reveal information about the orientation of the transition dipole moment in organic emission layers, which is one of the most important parameters defining the efficiency of organic light-emitting diodes. In this work, a refinement of one of the main experimental configurations utilized for such orientation measurements is presented. The technique is based on a step-by-step rotation of the optically excited layer with respect to the detector. By attaching the sample to a large glass half cylinder, the light initially trapped in the substrate can be extracted. It is shown that by inserting two additional optical lenses between the half cylinder and the detector, the signal-to-noise ratio can be improved by about one order of magnitude. A ray-optics model is derived that describes the light propagation in the macroscopic setup and enables us to characterize the impact of deviations from theoretical ideal measurement configurations. The numerical predictions are experimentally validated analyzing quantum-dot emission layers as an isotropic reference and established organic emitter molecules with well-known orientation values.

DOI: [10.1103/PhysRevApplied.14.064036](https://doi.org/10.1103/PhysRevApplied.14.064036)

I. INTRODUCTION

Angle-resolved photoluminescence spectroscopy (ARPS) is a fundamental technique used to study the properties and effects of light-emitting thin-film structures. A main application of this method is the investigation of exciton-polaritons and polariton condensation in microcavities comprising conventional [1,2] or organic [3,4] semiconductors, enabling the realization of optically [5] and electrically [6] driven polariton lasers. Another research topic utilizing ARPS is the investigation of the position and orientation of light-emitting molecules in organic thin films. In this case, the angular-intensity distribution is defined by the interference of light waves reflected multiple times at the sample interfaces. Hence, through knowledge of the layer thickness and optical constants of a specific sample, ARPS can reveal information about highly diluted emitters incorporated into nonemissive host materials.

A basic problem that limits the evaluation of angular spectra is a potentially higher refractive index of the emission layer compared to its environment, e.g., air. This

causes partial trapping of light due to total internal reflection for emission angles above a critical angle θ_{crit} with respect to the interface normal. Usually, such thin layers are deposited onto a thick substrate, often consisting of glass. In this case, due to the smaller refractive-index mismatch, the fraction of light penetrating the substrate is already much larger than the portion escaping to air. In this work, we focus on ARPS configurations that are capable of measuring the angular-emission pattern inside the substrate, since this ability is required for the application case discussed later on, which is the determination of emitter molecule orientations.

There exist two main experimental configurations to perform ARPS. The first is usually referred to as microphotoluminescence setup (μ -PL) and utilizes an objective lens with a large numerical aperture (NA) focused to a micrometer-sized spot on the sample surface. If the intensity distribution in the back-aperture plane is imaged onto a CCD camera, the angular-emission pattern can be recorded with one shot, enabling time-resolved measurements. Furthermore, the high lateral resolution allows for the imaging of isolated emitters diluted in thin films [7]. The drawback of this technique is its limited angle range, restricted by the NA of the objective used and resulting in cutoff angles of about 65° . The latter value corresponds to commercially available objectives with (NA = 1.4) and without (NA = 0.9) index-matching.

In this work, we focus on a second approach that is based on a step-by-step rotation of the sample with respect to

*sebastian.reineke@tu-dresden.de

Published by the American Physical Society under the terms of the [Creative Commons Attribution 4.0 International](https://creativecommons.org/licenses/by/4.0/) license. Further distribution of this work must maintain attribution to the author(s) and the published article's title, journal citation, and DOI.

a fix detector and allows us to resolve the complete forward emission distribution up to angles close to 90° . In this case, the substrate emission pattern can be extracted by attaching the sample to a large glass cylinder [8]. This iterative approach has the disadvantage of causing rather long measurement times, in the range of seconds or minutes. Nevertheless, due to its potential for addressing the complete angular spectrum and its rather simple-to-implement configuration, this is currently the most prominent technique for investigating the orientation of emitter molecules in organic thin films, as discussed in Sec. V.

Despite the widespread application of the second method, a quantitative evaluation of the impact of specific macroscopic setup designs on the measured angular spectra is missing so far. Here, we develop a ray-optics model in order to analyze possible systematic measurement deviations numerically and identify the most reliable realizations of the experimental setup. With that, our findings will help to improve the comparability of experimental results of different research groups.

As second main contribution of this work, we introduce a refinement of the state-of-the-art measurement configuration yielding an about one-order-of-magnitude higher signal-to-noise ratio (SNR). This enables us to address weakly emitting and fast-degrading materials.

Finally, as experimental validation, the orientation of organic emitter molecules and quantum dots is determined with both the conventional and the refined setup, resulting in consistent values.

II. NUMERICAL CALCULATION OF ANGULAR-EMISSION SPECTRA

A. Conventional and refined setup

In this section, the conventional and refined ARPS setups are introduced. They are schematically illustrated in Fig. 1. The sample consists of a light-emitting thin film deposited onto a glass substrate. The latter is attached to a glass half cylinder via index-matching oil. The cylinder is placed on top of a rotary stage, with its symmetry axis aligned to the rotation axis \hat{y} . The optical-excitation

source (not depicted) induces a small emission spot close to the \hat{y} axis but potentially shifted along \hat{z} due to the finite thick substrate, as discussed in Sec. II B. The conventional setup is completed by a small-area detector, often the aperture of an optical fiber connected to a spectrometer, located outside the cylinder at the same y position as the emission spot. The connection line between the detector and the \hat{y} axis defines the optical axis \hat{z} .

In this work, a refined setup configuration is developed that includes two additional lenses in front of the detector. The focus point of lens 1 coincides with the focus point of the half cylinder, causing a parallelization of all rays that initially propagate parallel to \hat{z} within the half cylinder. The detector is then placed at the focus point of lens 2, collecting all the parallelized rays. It has to be noted that the general direction of a light ray can be divided into two components, being parallel to either the horizontal x - z plane (red) or the vertical y - z plane (yellow). In case of the vertical component, the glass-air interface of the half cylinder is plane and, hence, causes no focusing. Nevertheless, lens 1 partially redirects oblique rays in the direction of the optical axis, which is the main reason for the enhanced SNR of the refined setup, as discussed in Sec. IV.

B. Ray-optics model

In the following, a ray-optics model is derived that describes the macroscopic incoherent propagation of light originating from a thin-film sample that is attached to a glass half cylinder. If the latter has optical properties similar to those of the sample substrate and both are well connected by index-matching oil, the situation can be simplified to an emission point $\vec{E} = (x_E, z_E)$ located inside of a cylinder that is centered at the origin of the coordinate system, as depicted in Fig. 2.

Under the assumption that the emission spot is not shifted too far away from the cylinder center ray, transfer analysis can be applied. The propagation of a ray that originates from a given position with distance x and angle θ with respect to the optical axis is described via the transfer

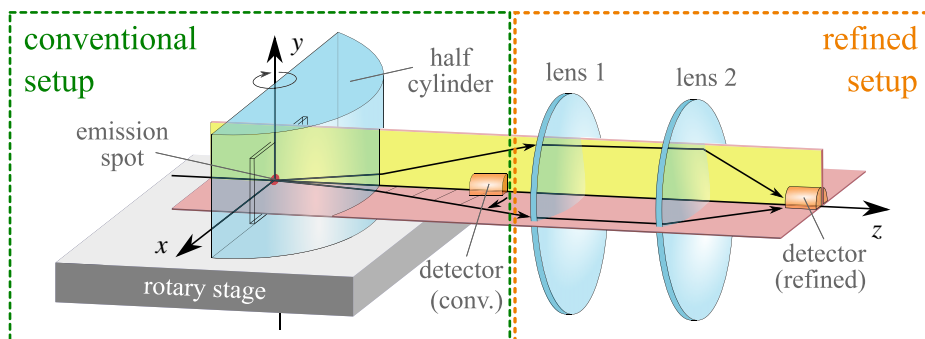


FIG. 1. A sketch of the conventional and refined ARPS setups with horizontal (x - z , red) and vertical (y - z , yellow) emission planes. The detector positions for both configurations are compared, showing that in the refined case a larger range of emitted rays is collected.

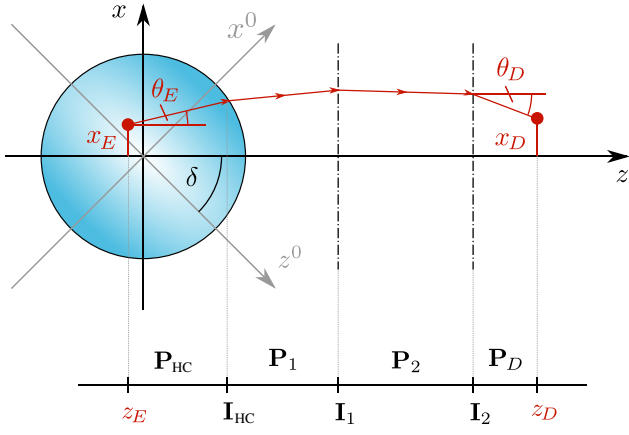


FIG. 2. A schematic illustration of the ray-transfer analysis as applied for the ARPS geometry. A ray (red) originates under an angle of θ_E from the emission point $\vec{E} = (x_E, z_E)$ located inside a glass cylinder (blue). The cylinder is rotated by an angle of δ with respect to its initial position, represented by the (x^0, z^0) coordinate system. The propagation to the detector position z_D is described by the propagation matrices \mathbf{P}_i and interface matrices \mathbf{I}_i .

matrix \mathbf{M} as [9–11]

$$\begin{pmatrix} x' \\ \theta' \end{pmatrix} = \mathbf{M} \begin{pmatrix} x \\ \theta \end{pmatrix}. \quad (1)$$

Depending on the optical environment between the initial and final positions, the matrix \mathbf{M} can assume arbitrary complex values for its 2×2 components. However, for special conditions such as propagation in a homogeneous medium or refraction at planes, thin lenses, or spherical interfaces, the respective transfer matrices can be derived analytically and are summarized in Appendix B. In general, the propagation of a ray can be divided into multiple sequential substeps i , each described by a submatrix \mathbf{M}_i . The overall propagation is then given by the sorted product of these submatrices, with the first step submatrix corresponding to the last factor:

$$\mathbf{M} = \prod_{i=N}^1 \mathbf{M}_i = \mathbf{M}_N \cdot \dots \cdot \mathbf{M}_1. \quad (2)$$

For the case of ARPS, the propagation will start at the emission point \vec{E} , with an emission angle θ_E inside of the half cylinder, which usually consists of glass. In the following, the z axis is aligned along the optical axis and contains the half-cylinder center M_{HC} as well as the detector position D . Hence, the light first propagates within glass which is described by the propagation matrix \mathbf{P}_{HC} . Then, it passes the cylinder-air interface represented by the interface matrix \mathbf{I}_{HC} . After that, the ray further propagates in air

and possibly passes further optical elements such as optical lenses. Thus, the following propagation is a product of additional propagation \mathbf{P}_i and interface \mathbf{I}_i matrices.

At the z position of the detector, the ray coordinates (x_D, θ_D) can then be calculated as

$$\begin{pmatrix} x_D \\ \theta_D \end{pmatrix} = \mathbf{P}_D \left(\prod_{i=N}^1 \mathbf{I}_i \mathbf{P}_i \right) \mathbf{I}_{\text{HC}} \mathbf{P}_{\text{HC}} \begin{pmatrix} x_E \\ \theta_E \end{pmatrix}. \quad (3)$$

Here, N denotes the number of additional optical components between the half cylinder and the detector and \mathbf{P}_D describes the propagation between the last optical component and the detector position.

In order to describe the general case of a rotated sample, a new coordinate system (x, z) needs to be introduced, which is rotated by an angle δ with respect to the initial coordinate system (x_0, z_0) , as depicted in Fig. 2. Then, the coordinates of the emission point change to

$$\vec{E}(\delta) = \begin{pmatrix} x_E(\delta) \\ z_E(\delta) \end{pmatrix} = \begin{pmatrix} \cos(\delta) & -\sin(\delta) \\ \sin(\delta) & \cos(\delta) \end{pmatrix} \cdot \begin{pmatrix} x_E^0 \\ z_E^0 \end{pmatrix} \quad (4)$$

and the effective emission angle θ in the rotated system is given by $\theta = \theta^0 - \delta$, where θ^0 is the angle in the initial coordinate system.

Furthermore, the cylinder itself might be displaced with respect to the rotation axis. Its symmetry axis $\vec{M}(\delta)$ then also depends on the current rotation angle δ and its surface is no longer necessarily symmetric to the optical axis. However, such a situation can still be treated using the already introduced formalism by a split description of the propagation in two coordinate systems, one centered at the cylinder midpoint and one having its origin at the rotation axis. The detailed steps of such a calculation are summarized in Appendix A.

Finally, it has to be considered that in real ARPS measurements, the light-emitting film is not deposited directly on the half cylinder but on a substrate that is attached to the half cylinder's plane side with the help of index-matching oil. In general, the refractive indices of the substrate and the half cylinder might differ. The resulting refraction at their common interface leads to a change of the angular-emission pattern, which is already included in the calculation of the ideal spectrum. In the calculation of the macroscopic ray propagation, this additional refraction also has to be taken into account, since it causes a displacement of the ray. However, since the substrate thickness is usually much smaller than the cylinder radius, this effect is very small and can be neglected in most cases, as discussed in Sec. V of the Supplemental Material [12].

C. Alteration of angular spectra

In nonideal measurement configurations, meaning that either the emission spot and/or the cylinder midpoint are

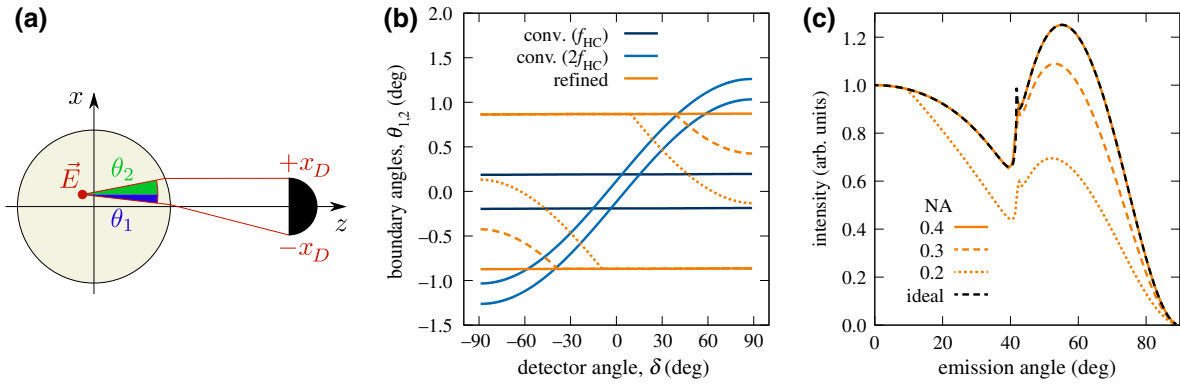


FIG. 3. (a) A sketch of the measurable angle range $[\theta_1, \theta_2]$ for a given emission spot \vec{E} and a detector [extension $[-x_D, +x_D]$]. In the case of a rotated cylinder, the angles θ_i describe the deviation from the given detector angle δ . (b) The calculated boundary angles θ_i for a displaced emission spot $E_{z_0} = -2$ mm with a half cylinder of radius $R_{\text{HC}} = 20$ mm and a detector aperture of $400 \mu\text{m}$. Five setup configurations are compared. For the conventional geometry, the detector is placed either at the cylinder's focus position f_{HC} (dark blue) or at the doubled focal length $2f_{\text{HC}}$ (light blue) with respect to the cylinder surface. The latter shows a much stronger dependency on the detector angle. The calculation also takes the maximal acceptance angle of the detector into account. This can lead to a cutoff of the measurable angles—as, for example, shown for the refined setup (orange). Here, the angle range is narrowed considerably for a small (dotted) and medium (dashed) compared to a large (solid) detector aperture. (c) The resulting angular spectra for the refined setup (orange), with three different NAs of the detector compared to the ideal spectrum (black).

displaced from the rotation axis or the detector has a finite aperture, at least part of the detected light rays is refracted at the cylinder surface. In other words, in such a case, the initial emission angle θ is different from the detector rotation angle δ . Moreover, in the case of an extended detector, a bunch of rays with emission angles in the range $[\theta_1, \theta_2]$ hits the finite detector aperture and contributes to the measured intensity. The two boundary angles θ_1 and θ_2 correspond to rays ending exactly at the left and right aperture edges, as illustrated in Fig. 3(a). Calculated boundary angles for both setup geometries and an emission-point displacement along the substrate normal of $E_{z_0} = -2$ mm are depicted in Fig. 3(b).

The intensity collected by the detector is then given by integrating the ideal angular spectrum over the boundary angle range. An extended emission spot is treated by integrating over the corrected angular spectra from all emission points \vec{E}' in the vicinity of the spot-center \vec{E}_c . The contributions from different emission points \vec{E}' are weighted by a function $w(\|\vec{E}' - \vec{E}_c\|)$, which can, for instance, be a Gaussian function to model optical excitation or a simple box function to describe the homogeneous emission of an electroluminescent sample. Finally, the corrected angular intensity I_{corr} can be derived from the ideal emission spectrum I_{ideal} as

$$I_{\text{corr}}(\delta) = \int dE' w(\|\vec{E}' - \vec{E}_c\|) \int_{\delta+\theta_1(\delta, \vec{E}')}^{\delta+\theta_2(\delta, \vec{E}')} d\theta I_{\text{ideal}}(\theta). \quad (5)$$

A comparison of the transverse magnetic (TM) polarized emission of an ideal and a corrected angular spectrum of

a 50-nm-thick isotropically emitting absorption-free layer with a refractive index of $n_{\text{org}} = 1.8$ on a glass substrate with $n_{\text{glass}} = 1.5$ is given in Fig. 3(c). The calculation is done for the refined setup, using the same emission spot displacement $E_{z_0} = -2$ mm as before. Additionally, different limited acceptance angles of the detector are taken into account, showing that in the case of a too small NA, a strong alteration in the larger angle range can be observed.

III. METHODS

A. Materials and sample preparation

In this work, single emission layers with thicknesses from a few tens of nanometers to about 100 nm are investigated. Two different types of materials are compared. On the one hand, quantum-dot (QD) layers of CdSe/CdS (core plus shell) with organic ligands are analyzed. They are prepared by a simple spin-coating process. The synthesis of these nanoparticles is done as described in Ref. [13]. Four different spin speeds (1600 rpm – 4500 rpm) lead to various layer thicknesses between about 20 nm and 80 nm.

On the other hand, doped organic emission layers are produced via physical-vapor deposition with the help of a ultrahigh-vacuum evaporation tool (Kurt J. Lesker Co., Germany) with chamber pressures of $< 10^{-7}$ mbar. The doping is realized by coevaporation of both the host and the guest material. Shadow masks are applied in order to shape the evaporated area and to allow it to simultaneously produce 6×6 samples on one wafer. To ensure a more homogeneous thickness distribution between the different samples on the wafer, the latter is continuously rotated during the evaporation. The layer thickness is monitored with

help of a quartz-crystal microbalance, located above the crucibles that contain the organic material powder. After finishing the evaporation process, the produced layers are encapsulated under a nitrogen atmosphere in order to prevent an exposure to oxygen and water and, hence, to enable long-term stability of the materials.

For both material types, the same particularly smooth substrate glass (Eagle XG glass, Thin Film Devices Inc., USA) is used. It has a thickness of 1.1 mm and it allows us to produce layers of very low surface roughness. It has a refractive index of around $n_{\text{XG}} = 1.52\text{--}1.51$ in the visible range.

Two organic emission layer systems, the orientation parameters of which are well known [14–21], are investigated in this work. The first consists of the host material N,N' -di(naphthalen-1-yl)- N,N' -diphenylbenzidine (NPB) and is doped by the red phosphorescent emitter iridium(III)bis(2-methylbenzo-[f,h]chinoxaline) (acetylacetonate) $[\text{Ir}(\text{MDQ})_2(\text{acac})]$. The host of the second system is 4,4'- N,N' -dicarbazole-biphenyl (CBP). It is doped with the green phosphorescent emitter bis(2-phenylpyridine)iridium(III)acetylacetonate $[\text{Ir}(\text{ppy})_2(\text{acac})]$. For both systems, the doping ratio is set to 8 wt%.

B. ARPS setup and measurement

In this work, two different ARPS setup configurations are compared. Both share as central element a rotary stage (OWIS, Germany), serving as platform for a glass half-cylinder lens with a radius of $R_{\text{HC}} = 20$ mm. Its symmetry axis is aligned to the rotation axis with the help of an adjustment laser that at the same time defines the optical axis. The samples are attached to the flat side of the half cylinder with help of Immersol index-matching oil (Zeiss, Germany). They are optically excited under an angle of 0° by a dot-laser module (Roithner, Germany) with a central wavelength of 405 nm. The spot size is set to around 1 mm and the spot center is aligned to the rotation axis with the help of the adjustment laser. The emission is detected with a USB2000 spectrometer (OceanOptics, USA), with an attached fiber of 400 μm core diameter and $\text{NA} = 0.2$. A PGT5010 Glan-Taylor polarizer (CASIX, China) is used to select either the TM- or the TE-polarized light. It is placed either directly in front of the spectrometer fiber head in the case of the conventional setup or between the two additional lenses in the refined geometry. It is aligned perpendicular to the optical axis using the back reflex of the adjustment laser. Furthermore, an edge filter ($\lambda_{\text{edge}} = 435$ nm) is used to block the excitation light.

For the conventional ARPS setup, the distance between the rotation axis and the spectrometer fiber head is varied between 2 cm and 12 cm. The refined setup includes the planoconvex aspheric lens AL2550M-A (Thorlabs, USA) with a focal length of $f_1 = 50$ mm, which is positioned at a distance of 11 cm from the rotation axis in order to

overlap its focus point with the half cylinder's focus point. Additionally, in this case, the fiber-port system PAF2S-11A (Thorlabs, USA) is used to collect the light previously parallelized by the first planoconvex lens. This system includes a second aspheric lens with a focal length of $f_2 = 11$ mm and is placed at a distance of 31 cm with respect to the rotation axis. The experimental and simulation input parameters of both setups are summarized in Table S6, in the Supplemental Material [12].

In order to detect a possible change of the overall emission of a specific sample during the measurement—for instance, because of sample degradation or setup drifts—its spectrum is recorded after every tenth measurement step at the reference angle $\delta_{\text{ref}} = 10^\circ$. The dependency of the intensity maxima with respect to the measurement step is fitted by an exponential or linear function. The inverse of the determined dependency is applied as a correction function to the complete experimental angular spectrum—as, for example, shown in Sec. VII of the Supplemental Material [12].

C. Numerical approximation of angular-emission spectra

The measured angular-emission spectra of the optically excited thin films are numerically approximated with help of an in-house-developed simulation tool. The calculation of the ideal spectral radiant intensity (SRI) is based on the formalism developed by Furno *et al.* [22]. It uses the thickness and the anisotropy coefficient of the involved emission layer as variation parameters. The optical constants, the thin-film photoluminescence spectrum, and the emission profile are required as input values. The latter is obtained by calculating the intensity profile of the excitation light along the substrate normal within the emission layer. This is done by applying the same transfer-matrix algorithm as utilized for the SRI calculation, which includes the absorption and multiple reflections of the incident light, resulting in a steady interference pattern. Assuming a spatially homogeneous excitation probability of the active layer, the obtained profile can be directly regarded as emission profile. To represent a spatially extended emission layer, the resulting angular spectra of several dipoles distributed homogeneously over the whole layer are superimposed. A specific emission profile can then be modeled by weighting the contributions of each dipole depending on its position within the layer.

The deviation from the ideal angular spectrum due to geometrical nonidealities of the setup is calculated as described in Sec. II C. In this case, further parameters such as the position of the emission spot \vec{E}_0 and the characteristics and positions of the lenses and the detector need to be defined or—if desired—varied.

In order to find a good approximation of the simulated SRI I_{sim} to the experimentally determined SRI I_{exp} , the

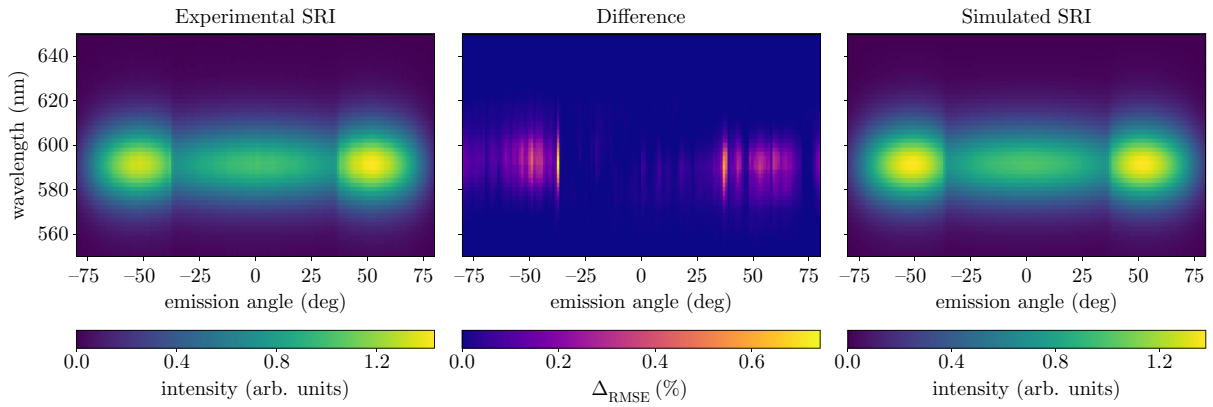


FIG. 4. The experimental (left) and simulated (right) angular-emission spectra of a QD layer (3300 rpm). The center plot shows the residual map of the best fit (right), which is determined by variation of the film thickness and the anisotropy coefficient and setup parameters such as the excitation spot and half-cylinder displacement.

root-mean-square error (Δ_{RMSE}) is minimized by varying the chosen parameters using a simplex algorithm [23]. The deviation criterion is defined as

$$\Delta_{\text{RMSE}} = \sqrt{\sum_{i,j} [I_{\text{exp}}(\lambda_i, \delta_j) - I_{\text{sim}}(\lambda_i, \delta_j)]^2}. \quad (6)$$

As an example, the measured and calculated SRI of a QD layer is depicted in Fig. 4. Additionally, in the middle graph, the residual map is shown, the sum of which yields the final Δ_{RMSE} value of this specific fit.

D. Variable-angle spectroscopic ellipsometry

The optical constants of all thin-film materials as well as for the glass substrate and the half cylinder are determined by variable-angle spectroscopic ellipsometry (VASE) with the tool EP4 (Accurion GmbH, Germany). The ellipsometric parameters Δ and Ψ are measured for multiple angles of incidence in the range of $50\text{--}60^\circ$ in case of glass substrates and in the range of $60\text{--}70^\circ$ if silicon substrates are used. Whenever glass substrates are investigated, their backside is covered with black tape in order to reduce the noise caused by the reflection at the backside. From the measured ellipsometric parameters, the optical constants are determined with the software tool EP4Model (Accurion GmbH, Germany). An elaborate dispersion is expressed as the superposition of a constant real offset of $n = 1.0$, UV poles, and Gaussian oscillator term. The amplitudes, widths, and energetic positions of the latter serve as fitting parameters. For the substrate glasses and the QD layers, isotropic optical constants are identified. In case of the organic material systems, effective isotropic dispersions are calculated from uniaxial models having a small anisotropy between the in-plane and out-of-plane direction. This is consistent with the results of Yokoyama *et al.* [24], which show similar dependencies for the two

host materials NPB and CBP. A complete overview of the determined refractive indices is given in Sec. I of the Supplemental Material [12].

IV. ENHANCED SIGNAL-TO-NOISE RATIO

One of the main advantages of the refined setup is the improved SNR, which is about one order of magnitude higher compared to the conventional configuration, as shown in Fig. 5. In this section, the reason for this observation is discussed.

As already mentioned in Sec. II A, in the real three-dimensional space, light rays can also propagate downward and upward in a vertical plane depicted in yellow

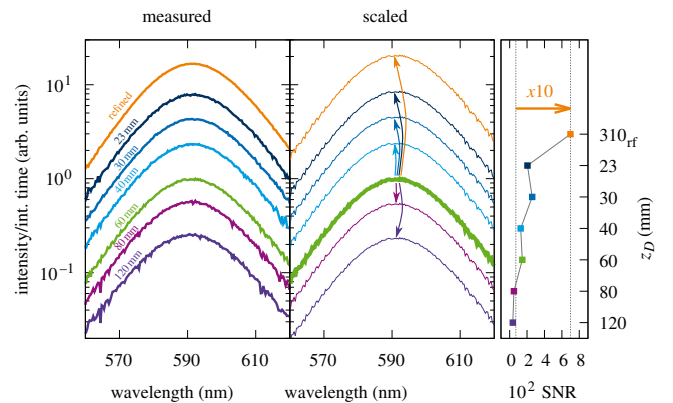


FIG. 5. The measured (left) and, by the product of the boundary angles, scaled intensities (center) for different detector positions (z_D) at an emission angle of 10° . In the center graph, the spectrum measured at $z_D = 60$ mm (detector in cylinder focus) is taken as the reference and all other spectra are obtained by multiplying the respective scale factor s given in Table S5, in the Supplemental Material [12]. The orange lines show the spectra of the refined setup (rf), which increases the SNR (right) by about one order of magnitude.

in Fig. 1. In this projection, the cylinder-air interface is just a plane. Hence, initially downward-propagating light will further propagate downward after this interface with an increased propagation angle due to the refraction. This implies that an extended detector placed directly at the cylinder surface will measure a larger range of slightly oblique rays than a detector moved away from the cylinder. In contrast, if the refined setup geometry is applied, the additional spherical lenses L_1 and L_2 will partly collect nonparallel rays and focus them to the detector. In sum, this leads to much higher measurable intensities when using the refined setup, with the angular resolution kept very high. In principle, the latter statement needs to be confirmed by a two-dimensional ray transfer analysis, which is not done in this work. However, a simple calculation of the boundary angles in the perpendicular plane with an ideal emission spot and cylinder position shows that the angular broadening is comparably small ($< 1^\circ$) and should not have much impact on the angular spectra. By multiplying the calculated horizontal and vertical boundary angles, the two-dimensional angular integration area can be estimated for different setup configurations. This integration area should be a measure for the detectable intensities in the different configurations. The left-hand graph of Fig. 5 shows measured spectra of a QD sample at $\delta = 10^\circ$ for different detector positions in the conventional setup and one position of the refined setup (orange). It is obvious that the intensity decreases considerably when moving the detector away from the sample. Interestingly, the highest signal is achieved when using the refined setup. This observation can be quantified by calculating the SNR for each configuration, which is depicted in the right-hand plot of Fig. 5 and indicates an enhancement of about one order of magnitude. For comparison and in order to validate the ray-optics model, the spectrum measured at $z_D = 60$ mm (green) is multiplied by the calculated angle integration area for each of the other configurations. The resulting scaled spectra reproduce the experimental dependency very well, as depicted in the center graph of Fig. 5.

V. MEASUREMENT OF EMITTER ORIENTATION

A. Horizontal emitters as OLED efficiency boosters

As a key player in today's display industry and a major candidate for future lighting technologies, organic light-emitting diodes (OLEDs) represent an impressive example of the significant impact that applied physics can make on everyday life. Although state-of-the-art OLEDs already fulfill industrial display performance requirements, their overall efficiency needs to be further increased to allow for efficient applications in the field of high-brightness light sources. In particular, their ability to transfer the internally generated light to the outside of the device is currently a limiting factor, mainly caused by the high refractive index of the organic layers. One of the most important

approaches to reducing this loss channel is to align the transition dipole moments (TDM) of the light-emitting molecules parallel to the layer interface planes. Then, total internal reflection as well as coupling to plasmonic loss modes can be minimized and the device efficiency can be enhanced by about 50% [8] compared to an isotropic distribution. Such an optical-performance boost is directly translated to the external quantum efficiency (η_{EQE}) of an OLED, even for prime devices with a perfect charge-balance factor γ , a radiative exciton fraction of $\eta_r = 1$, and a high radiative quantum efficiency q_{eff} resulting in an internal quantum efficiency (η_{int}) close to 100% [25]. Then, the η_{EQE} is almost solely determined by the optical outcoupling efficiency η_{out} :

$$\eta_{\text{EQE}} = \gamma \eta_r q_{\text{eff}} \eta_{\text{out}} = \eta_{\text{int}} \eta_{\text{out}} \approx \eta_{\text{out}}. \quad (7)$$

In order to find experimental methods to control the TDM orientation, a precise and reliable measurement technique for this material property is indispensable. The progress in the field of molecular orientation has been reviewed recently by Schmidt *et al.* [14] and Kim *et al.* [26]. In both papers, it is stated that ARPS has emerged to be currently the most prominent technique in terms of the experimental determination of the molecular orientation. Compared to VASE [27], it has the clear advantage of being sensitive to small fractions of emitter molecules doped into a host material, as often present in efficient OLEDs. Angle-resolved electroluminescence measurements [16,28] can also reveal the TDM orientation by analyzing OLEDs in the optical minimum. The latter refers to a set of layer thicknesses that suppresses the contribution of horizontal dipoles by destructive interference in order to make the small light fraction originating from vertical dipoles measurable. However, this approach not only requires a higher effort in sample design but also includes many more experimental parameters, which entail more potential uncertainties in optical modeling. Another approach is based on the analysis of photoluminescent exciton decay rates and quantum yields, which are directly related to the TDM orientation via the Purcell factor [29,30]. Since this method addresses different experimental quantities, it could be used as a complementary crosscheck in a detailed investigation. However, it is also a rather complex technique that requires the fabrication of multilayer samples, the accurate measurement of two quantities, and optical modeling.

B. Light emission of oriented dipoles in thin films

The experimental method to determine the orientation of emitter molecules via ARPS was initially proposed by Frischeisen *et al.* [8]. It is a two-step approach that requires, first, the experimental recording of the angular-emission spectra and, second, a numerical fit of such data sets that includes the TDM orientation as a fitting

parameter. The theoretical formalism used to calculate the angular-radiation pattern of thin emission layers on glass substrates is described by Furno *et al.* [22]. It is based on a classical electromagnetic model treating the emission of excited (molecular) states as radiation of electrical dipole antennas altered by the surrounding planar multilayered structure. An arbitrarily oriented dipole is described as the superposition of in-plane (\parallel) and out-of-plane (\perp) dipoles emitting TM and transverse-electric (TE) polarized light. The resulting overall far-field emission $I(\theta, \lambda, a)$, where θ is the emission angle relative to normal emission and λ refers to the vacuum wavelength, is given as

$$I(\theta, \lambda, a) = aI_{\perp, \text{TM}} + (1 - a)(I_{\parallel, \text{TM}} + I_{\parallel, \text{TE}}). \quad (8)$$

Here, the differently oriented dipoles are weighted by the anisotropy coefficient a , which is defined as the relative contribution of out-of-plane dipoles. Since this factor quantifies the dipole alignment relative to the substrate normal, from here on it is referred to as the orientation parameter. It ranges from zero to one, covering all ratios from only in-plane to only out-of-plane dipoles, respectively, where the value of one third describes an isotropic distribution. It has to be pointed out that the scalar anisotropy coefficient cannot contain complete information about the dipole distribution but quantifies the ensemble average of the orientation. An illustrative discussion of its relation to the actual distribution is given in Sec. VIII of the Supplemental Material [12].

In order to sensitively probe the dipole orientation, the contributions of both in-plane and out-of-plane dipoles have to be balanced. For this purpose, two measures are adopted. First, solely TM-polarized light is recorded, which excludes the second in-plane term in Eq. (8). Second, it is essential to enhance the measurable contribution of out-of-plane dipoles. Since they mainly emit to large angles, most of their emission is trapped inside the emission layer and glass substrate due to total internal reflection. By attaching the sample to a large glass half-cylinder lens, it is possible to overcome at least the substrate losses. Under the assumption of an infinitely small emission spot located at the half cylinder's symmetry axis, every emitted light ray hits the half-cylinder surface perpendicularly and will not be refracted. A point detector placed outside the half cylinder will then measure the same angular-emission dependence as is present inside the sample's substrate.

C. Numerical characterization of experimental uncertainties of the conventional setup

In general, a precise and comparable measurement technique requires a detailed understanding of the specific setup characteristics, especially its nonidealities and their impact on the resulting measurement value. Deviations of some setup parameters might lead to significant changes of the outcome, while others might have negligible effects.

In the case of investigation of the emitter orientation by ARPS, the microscopic analysis of the angular-radiation pattern has been performed and evaluated carefully. Different sample architectures have been compared [8,15,31], the importance of utilizing precise optical constants has been pointed out [32,33], and also the impact of anisotropic optical constants of the emission layer has been taken into account [34–36]. The emission profile along the out-of-plane direction has been carefully investigated for electroluminescence measurements [18,37] and, in some studies, is also addressed in the modeling of photoluminescent spectra [15].

On the other hand, a thorough examination of the impact of macroscopic setup parameters is missing so far. A crucial point in the numerical approximation of experimental data determined by ARPS is the assumption that this method yields the angular spectra as present in the sample's substrate, which usually consists of glass. By attaching this glass substrate to a glass half cylinder and positioning a very small emission spot at the half cylinder's center axis, it can be guaranteed that all emitted light rays hit the cylinder surface perpendicularly and, hence, are not refracted at the glass-air interface. Then, a detector placed in front of the half cylinder perfectly records the angular emission as being within the sample's substrate.

In this section, the impact of deviations from this ideal configuration on the resulting orientation value are investigated numerically. This enables us to uncover systematic measurement deviations, to quantify uncertainties due to experimental accuracy limitations, and to design the ARPS setup in the most proper way.

In order to reveal the impact of nonidealities of different specific setup configurations, in the following, non-ideal angular spectra are calculated using the approach as described in Sec. II C. These calculated spectra are then fitted with the assumption of an ideal setup configuration, meaning without displacement of the emission spot and half cylinder as well as having a point emission spot and a point detector. If the alteration due to the nonideality is small, the resulting anisotropy coefficient should be close to the one that is given initially. Figure 6 shows the respective dependencies for an isotropically emitting absorption-free layer with a refractive index of $n_{\text{org}} = 1.8$ on a glass substrate with $n_{\text{glass}} = 1.5$.

The impact of two macroscopic parameters, the half-cylinder radius and the distance between the sample and the detector, is tested. For all configurations, five different emission-point positions E_{z0} are compared, which correspond to a displacement along the substrate normal. Experimentally, this shift could, for instance, be induced by varying the substrate thicknesses. The lateral spot position E_{x0} is kept at the ideal value of zero.

In the two graphs of Fig. 6, the resulting anisotropy coefficients for two different cylinder radii, $R_{\text{HC}} = 20$ mm

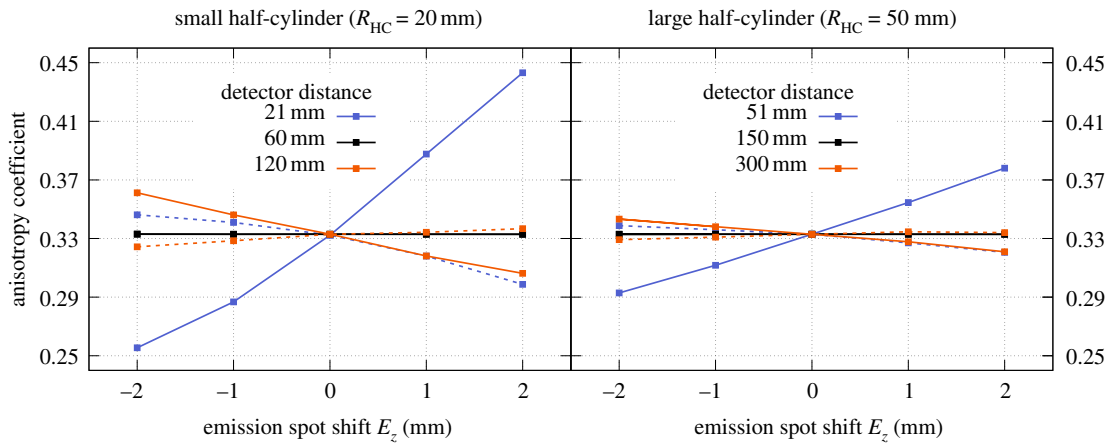


FIG. 6. Fitted anisotropy coefficients assuming ideal angular emission but using calculated nonideal spectra as input data. The dependence for a shift of the emission spot along the substrate normal E_z is compared for a smaller (left) and a larger (right) half-cylinder radius R_{HC} . The detector is located directly in front of the half-cylinder surface (blue), at its focus point (black), or at the twofold focal length (orange). The fit is either performed by optimizing the layer thickness (solid) or by keeping it constant at the nominal thickness (dashed).

(left) and $R_{\text{HC}} = 50$ mm (right), are compared. In both cases, the detector is placed directly in front of the cylinder surface (blue), at the cylinder's focus point (black) or at the doubled focal length (orange). In general, the spot-position dependency is lower for the larger cylinder. Also, if the layer thickness is not fitted but kept at the nominal value (dashed lines), the variation is drastically decreased. Most importantly, by placing the detector at the cylinder's focus point, the spot-position dependency can be almost completely eliminated, independent of the cylinder size. Hence, from the numerical point of view, this is the best detector position in terms of the stability of measured angular spectra versus displacements of the emission spot. In contrast, if the detector is placed outside the cylinder focus, it is only in the case of an emission spot perfectly aligned at $E_z = 0$ mm that the right anisotropy coefficient is fitted. A displacement of $E_z = -1$ mm, which could be caused by using 1-mm-thick substrate glass, results in an over- or underestimation of the anisotropy coefficient by up to about $\Delta a = 0.04$ for the small and $\Delta a = 0.02$ for the large cylinder. The most unfavorable situation is given if the detector is positioned directly in front of the cylinder surface. Then, in case of the small cylinder, the fitted anisotropy values range from $a = 0.26$ to $a = 0.44$ for $E_z = -2$ mm to $E_z = +2$ mm when fitting the thickness and still cover the range from $a = 0.35$ to $a = 0.30$ when using the nominal thickness of 50 nm. Taking into account that the measurement uncertainty of ARPS is often stated to be in the range $\Delta a = \pm 0.02$ [18,19,33], this dependency can have a significant influence on the scattering of the literature values.

The numerically predicted impact of the emission-spot position is proven experimentally for different detector positions as summarized in Sec. III of the Supplemental

Material [12]. Furthermore, the impact of lateral displacements of both the emission spot ($E_{x0} \neq 0$) and the cylinder symmetry axis ($M_x \neq 0$) is calculated. The results are given in Sec. IV of the Supplemental Material [12].

D. Advantages of the refined setup

The previous section clearly shows that from the numerical point of view, the most stable and reliable configuration of an ARPS setup is given when placing a small detector at the focus of the half-cylinder lens. However, in real experimental conditions, this realization is not always viable and can even cause large deviations from the expected spectra. The reason for this is the necessary application of polarizing optics in order to filter out the unwanted TE modes from the overall signal. The extinction ratio of such polarizers can be extremely sensitive to the angle of incidence of the light rays. On the other hand, in the case of displaced emission spots, the propagation angle of the light rays will be larger for larger detector angles because the spot is moved away from the optical axis when turning the sample. As a consequence, there is a chance that the polarizer will work worse in the higher-detector-angle range and, hence, the transmitted TE fraction will be enlarged. This leads to an overestimation of the measured intensities and, thus, to a wrong anisotropy coefficient. If there is an additional lateral displacement of the cylinder or the emission spot, this dependency might even be intensified for one of the angle branches, causing massive asymmetries of the measured spectra.

In contrast, the refined setup has the advantage that all necessary optics, including the polarizer, can be placed in the space between the two lenses, where the light rays are close to parallel to the optical axis. This might be a

crucial requirement to guarantee a reliable performance of, for example, high-extinction-ratio Glan-Taylor prisms with small acceptance angles. Another practical advantage is the possibility of using integrated fiber incoupling systems for the unit of the second lens and detector. They often allow us to very precisely position the fiber head in the lens focus in order to maximize the measured signal.

In terms of deviations from the ideal angular spectrum, there is, in principle, no difference between the conventional and the refined setup, since the latter effectively just images the signal at the half-cylinder focus position to the detector. This can be shown by calculating the boundary angles for both configurations. For infinitely small detectors, the angle dependency is exactly the same, namely, giving just the ideal spectrum. However, for extended detectors, the range of detected parasitic rays depends on the specific lens parameters and can be either broadened or narrowed. For the setup configuration used in this work, the boundary angle range is slightly broadened but still in an acceptable resolution range of $\pm 1^\circ$ as, for example, shown in Fig. 3(b).

E. Anisotropy coefficient of isotropic quantum-dot films and established organic emitters

In the past decade, ARPS has mainly been applied to determine the orientation of small organic emitter molecules that either form neat layers or are embedded inside an organic host material. One of the main problems in this context is that it is difficult to choose a material system that can serve as a perfectly isotropic emitting reference. Although many small molecules have a bulky ball-like shape, the possibility cannot be excluded that they nevertheless exhibit a small net orientation of their TDMs due to interactions of the ligands or small deformations when embedded in a solid layer. A much more reliable candidate for real isotropic emission are spherical QDs. Due to their almost perfect ball shape, equal-emission probabilities in all directions can be expected and have been measured [32].

Hence, in this work, neat layers of CdSe/CdS are analyzed as possible isotropic reference systems. Figure 7 shows TM- (blue) and TE-polarized (orange) angular spectra of such a sample at the peak wavelength of 590 nm, recorded with the refined setup (dots). Furthermore, the respective fitted spectra are depicted as lines. Throughout this section, in order to save computational time, the numerical approximation of experimental data is restricted to the wavelength of the thin-film emission maximum in the forward direction. This constraint causes only very small deviations compared to a fitting of the whole emission spectrum, as has previously been confirmed for a selection of data sets.

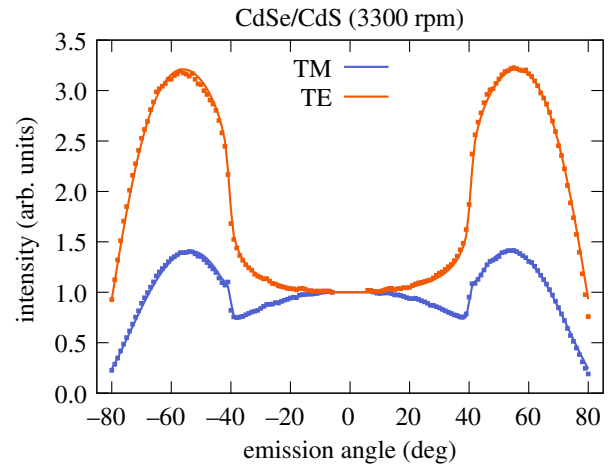


FIG. 7. The angular emission of a QD single layer at its peak wavelength (590 nm). Both TM- (blue) and TE-polarized (orange) contributions are measured and fitted using a common layer thickness. The determined anisotropy coefficient of $a = 0.343$ is very close to the isotropic value of $a = 1/3$.

The numerical approximation is done in two steps. First, a general screening of the impact of different setup parameters is performed by doing coupled fits of TM- and TE-polarized spectra of various samples. The displacement of the excitation spot with respect to the rotation axis is set to $E_{z0} = -1.1$ mm, which is in agreement with the substrate thickness. Two important parameters are identified, which are the z displacement of the half cylinder (M_{z0}) with respect to the rotation axis and the shift of the detector (Δz_D) with respect to the focus point of lens 2. The most consistent results for the whole set of data are achieved for $\Delta z_D = 0.2$ mm. Hence, this value is fixed in the following. It has to be noted that this displacement probably does not correspond to the real physical position of the detector fiber but, rather, represents an effective correction of all displacements of the optical components in the light path. The second parameter M_{z0} is fitted independently for each sample in the range of 0.5–1.5 mm, accounting for small experimentally possible shifts of the half-cylinder position. The determined M_{z0} values are listed in Table S2, in the Supplemental Material [12].

The measurement is performed for four QD samples of the same material prepared with different spin-coating speeds. The resulting average orientation values for both the conventional and the refined setup are listed in Table I. They are very close to the isotropic value of $a = 1/3$, which confirms the general reliability of the refined setup and also the applicability of the nonideality corrections. The single fitting results of each sample can be found in Sec. II of the Supplemental Material [12].

It is important to note that the fitted layer thicknesses agree well with the values determined by ellipsometry, having a deviation of less than 15% for all samples. Taking

TABLE I. The mean values and standard deviations of the determined anisotropy coefficients of multiple samples with different thicknesses. Measurements from both setup configurations are compared, yielding consistent orientation parameters that coincide with the literature values [14] within the range of measurement uncertainty.

Material	$a_{\text{conventional}}$	a_{refined}	a_{Lit}
CdSe/CdS	0.33 ± 0.02	0.35 ± 0.01	...
CBP:Ir(ppy) ₂ (acac)	0.23 ± 0.01	0.24 ± 0.02	0.23–0.24
NPB:Ir(MDQ) ₂ (acac)	0.24 ± 0.01	0.26 ± 0.02	0.23–0.25

into account that the two measurements are not necessarily done at the same spot of the spin-coated sample, this is a very low discrepancy.

Besides the previously described QD system, the TDM orientation of which has, so far, not been discussed very much in the literature, two standard iridium-based phosphorescent OLED emitters, resembling well-studied reference-material sets, are evaluated. Both are fabricated with four different nominal thicknesses between 20 nm and 110 nm. Again, for all samples, the TE- and TM-polarized emission spectra are recorded and approximated by a coupled fit varying the layer thickness and the anisotropy coefficient, the latter only for the TM-polarized spectra. The resulting averaged anisotropy coefficients are summarized in Table I and compared to the literature values [14], showing good agreement. The detailed fitting results can be found in Sec. II of the Supplemental Material [12].

It has to be pointed out that, especially for thicker samples, it is important to take the emission profile into account in order to obtain consistent values. It is calculated as described in Sec. III C and as shown, for example, in Fig. S9, in the Supplemental Material [12] for the four QD layers.

VI. CONCLUSION

In the present work, a refined setup for ARPS is introduced that utilizes two additional planoconvex lenses that image the half-cylinder focus point to the detector. It is capable of measuring the complete emission range up to angles of almost 90° and provides an approximately tenfold-increased SNR with respect to a comparable conventional configuration while retaining a high angular resolution. The enhanced sensitivity might facilitate the exploration of weakly emitting or fast-degrading materials that have not been addressable so far.

The improvement is caused by a parallelization of the light rays between the inserted lenses, compared to the divergent propagation in the conventional case. This strongly reduces the SNR dependency of the sample-detector distance z_D . For instance, the refined configuration realized in this work has a SNR of about 700 at $z_D = 31$ cm. In comparison, the SNR of the conventional setup

already drops from about 260 to 35 at much smaller distances of $z_D = 3$ cm to $z_D = 12$ cm. The considerable extension of the possible setup dimensions simplifies the practical handling of the experiment but may also enable us to extend the setup using further components for advanced measurements such as quarter- or half-wave plates in order to characterize polarization-dependent anisotropic emission. Additionally, there are practical advantages, such as exposing the optical components to mainly parallel light and finely adjusting the incoupling to the optical fiber by using integrated fiber port systems.

In order to characterize and compare specific ARPS configurations, a ray-optics model is derived that accounts for the macroscopic setup geometry. The developed equations are solved numerically and the deviation from the ideal angular spectra is calculated for different realistic experimental configurations. In particular, the impact of a displacement of the emission spot and/or the cylinder midpoint with respect to the rotation axis is probed for different configurations. The findings reveal substantial deviations of the resulting orientation parameter, even for small displacements. Especially in the case of varying substrate thicknesses, this issue might be hard to control. In the case of the conventional design, it is shown that placing the detector at the focus point of the half cylinder is the most stable configuration. Also, large cylinder radii reduce the impact of spot and cylinder displacements relative to the rotation axis.

Experimentally, both setup configurations are characterized with the help of isotropically emitting QD films as well as with established organic emitters, showing good agreement with previously published values. The applicability of the deduced formalism is demonstrated by comparing its predictions to measurements with intentionally displaced emission spots, as presented in Sec. III of the Supplemental Material [12]. Also, the measured intensity scaling for different detector positions can be calculated very accurately.

In this regard, this work might help to improve the comparability and precision of measured molecular orientations and, hence, enable us to understand the mechanisms influencing that property or, moreover, finding ways to control it. With that, it can be an important building block in research and development in the area of luminescent thin-film systems including OLEDs, quantum-dot LEDs, and perovskite LEDs.

ACKNOWLEDGMENTS

We acknowledge Christian Meerbach and Professor Dr. Alexander Eychemüller for preparing and providing the QD layers. C.H. thanks Andreas Hofacker for fruitful discussions regarding the optical simulations. C.H. acknowledges funding from the European Research Council under

the European Union's Horizon 2020 research and innovation program (Grant Agreement No. 679213; project acronym BILUM).

APPENDIX A: DISPLACED CYLINDER

Throughout this work, the position of the emission spot $\vec{E}_0 =: \vec{E}_0^M$ is always given with respect to the cylinder's symmetry axis \vec{M} . The analysis of the ray propagation in the case of a displaced cylinder ($\vec{M}_0 \neq \vec{0}$) is done in the following way. First, the given emission-point coordinates are translated to the rotational coordinate system R , yielding $\vec{E}_0^R = \vec{E}_0^M + \vec{M}$. Then, both the cylinder coordinate and the emission point are rotated by the given detector angle δ . The resulting emission point \vec{E}_δ^R is expressed with respect to the rotated cylinder coordinate \vec{M}_δ as $\vec{E}_\delta^M = \vec{E}_\delta^R - \vec{M}_\delta$. Then the ray propagation within the cylinder for a given emission angle θ is calculated as before, but using \vec{E}_δ^M as the emission-point coordinate. Finally, the derived crossing point \vec{P}_δ^M at the cylinder-air interface is translated back to the rotational coordinate system as $\vec{P}_\delta^R = \vec{P}_\delta^M + \vec{M}_\delta$. The following propagation including possible refractions at further lenses is evaluated as before in the rotational coordinate system.

APPENDIX B: ANALYTICAL TRANSFER MATRICES

In this appendix, a list of analytically derivable transfer matrices applied in this work is given [11]:

Optical system	Transfer matrix
Free space	$\mathbf{P} = \begin{pmatrix} 1 & L \\ 0 & 1 \end{pmatrix}$
Plane interface	$\mathbf{I}_{\text{plane}} = \begin{pmatrix} 1 & 1 \\ 0 & \frac{n_1}{n_2} \end{pmatrix}$
Thin lens	$\mathbf{I}_{\text{lens}} = \begin{pmatrix} 1 & 0 \\ -\frac{1}{f} & 1 \end{pmatrix}$
Spherical surface	$\mathbf{I}_{\text{HC}} = \begin{pmatrix} 1 & 0 \\ \frac{n_1 - n_2}{n_2 R} & 1 \end{pmatrix}$

The present parameters are the propagation distance L , the focal length f , the cylinder radius R , and the refractive indices n_1 and n_2 of the two media separated by the interface.

[1] J. Kasprzak, M. Richard, S. Kundermann, A. Baas, P. Jeambun, J. M. J. Keeling, F. M. Marchetti, M. H. Szymańska,

- R. André, J. L. Staehli, V. Savona, P. B. Littlewood, B. Deveaud, and L. S. Dang, Bose-Einstein condensation of exciton polaritons, *Nature* **443**, 409 (2006).
- [2] R. Balili, V. Hartwell, D. Snoko, L. Pfeiffer, and K. West, Bose-Einstein condensation of microcavity polaritons in a trap, *Science* **316**, 1007 (2007).
- [3] K. S. Daskalakis, S. A. Maier, R. Murray, and S. Kéna-Cohen, Nonlinear interactions in an organic polariton condensate, *Nat. Mater.* **13**, 227 (2014).
- [4] J. D. Plumhof, T. Stöferle, L. Mai, U. Scherf, and R. F. Mahrt, Room-temperature Bose-Einstein condensation of cavity exciton-polaritons in a polymer, *Nat. Mater.* **13**, 247 (2014).
- [5] S. Kéna-Cohen and S. Forrest, Room-temperature polariton lasing in an organic single-crystal microcavity, *Nat. Photonics* **4**, 371 (2010).
- [6] C. Schneider, A. Rahimi-Iman, N. Y. Kim, J. Fischer, I. G. Savenko, M. Amthor, M. Lerner, A. Wolf, L. Worschech, V. D. Kulakovskii, I. A. Shelykh, M. Kamp, S. Reitzenstein, A. Forchel, Y. Yamamoto, and S. Höfling, An electrically pumped polariton laser, *Nature* **497**, 348 (2013).
- [7] M. A. Lieb, J. M. Zavislan, and L. Novotny, Single-molecule orientations determined by direct emission pattern imaging, *J. Opt. Soc. Am. B* **21**, 1210 (2004).
- [8] J. Frischeisen, D. Yokoyama, C. Adachi, and W. Brütting, Determination of molecular dipole orientation in doped fluorescent organic thin films by photoluminescence measurements, *Appl. Phys. Lett.* **96**, 073302 (2010).
- [9] A. Gerrard and J. M. Burch, *Introduction to Matrix Methods in Optics* (Wiley, London, 1975).
- [10] H. Kogelnik and T. Li, Laser beams and resonators, *Appl. Opt.* **5**, 1550 (1966).
- [11] N. Hodgson and H. Weber, *Laser Resonators and Beam Propagation* (Springer Science+Business Media, New York, 2005).
- [12] See the Supplemental Material at <http://link.aps.org/supplemental/10.1103/PhysRevApplied.14.064036> for optical constants, measured and simulated angular spectra, simulation and setup parameters, calculations of the impact of imperfect index matching of the substrate, emission profiles, overall intensity changes, and discussions of the interpretation of the anisotropy coefficient and the thickness-orientation correlation.
- [13] V. Sayevich, C. Guhrenz, M. Sin, V. M. Dzhagan, A. Weiz, D. Kasemann, E. Brunner, M. Ruck, D. R. T. Zahn, K. Leo, N. Gaponik, and A. Eychmüller, Chloride and indium-chloride-complex inorganic ligands for efficient stabilization of nanocrystals in solution and doping of nanocrystal solids, *Adv. Funct. Mater.* **26**, 2163 (2016).
- [14] T. D. Schmidt, T. Lampe, M. R. D. Sylvinson, P. I. Djurovich, M. E. Thompson, and W. Brütting, Emitter Orientation as a Key Parameter in Organic Light-Emitting Diodes, *Phys. Rev. Appl.* **8**, 037001 (2017).
- [15] M. Flämmich, J. Frischeisen, D. S. Setz, D. Michaelis, B. C. Krummacher, T. D. Schmidt, W. Brütting, and N. Danz, Oriented phosphorescent emitters boost OLED efficiency, *Org. Electron.* **12**, 1663 (2011).
- [16] A. Graf, P. Liehm, C. Murawski, S. Hofmann, K. Leo, and M. C. Gather, Correlating the transition dipole moment ori-

- entation of phosphorescent emitter molecules in OLEDs with basic material properties, *J. Mater. Chem. C* **2**, 10298 (2014).
- [17] T. Lampe, T. D. Schmidt, M. J. Jurow, P. I. Djurovich, M. E. Thompson, and W. Brütting, Dependence of phosphorescent emitter orientation on deposition technique in doped organic films, *Chem. Mater.* **28**, 712 (2016).
- [18] P. Liehm, C. Murawski, M. Furno, B. Lüssem, K. Leo, and M. C. Gather, Comparing the emissive dipole orientation of two similar phosphorescent green emitter molecules in highly efficient organic light-emitting diodes, *Appl. Phys. Lett.* **101**, 253304 (2012).
- [19] S.-Y. Kim, W.-I. Jeong, C. Mayr, Y.-S. Park, K.-H. Kim, J.-H. Lee, C.-K. Moon, W. Brütting, and J.-J. Kim, Organic light-emitting diodes with 30% external quantum efficiency based on a horizontally oriented emitter, *Adv. Funct. Mater.* **23**, 3896 (2013).
- [20] K.-H. Kim, C.-K. Moon, J.-H. Lee, S.-Y. Kim, and J.-J. Kim, Highly efficient organic light-emitting diodes with phosphorescent emitters having high quantum yield and horizontal orientation of transition dipole moments, *Adv. Mater.* **26**, 3844 (2014).
- [21] C. Fuchs, P.-A. Will, M. Wiczorek, M. C. Gather, S. Hofmann, S. Reineke, K. Leo, and R. Scholz, Enhanced light emission from top-emitting organic light-emitting diodes by optimizing surface plasmon polariton losses, *Phys. Rev. B* **92**, 245306 (2015).
- [22] M. Furno, R. Meerheim, S. Hofmann, B. Lüssem, and K. Leo, Efficiency and rate of spontaneous emission in organic electroluminescent devices, *Phys. Rev. B* **85**, 115205 (2012).
- [23] J. A. Nelder and R. Mead, A simplex method for function minimization, *Comput. J.* **7**, 308 (1965).
- [24] D. Yokoyama, Molecular orientation in small-molecule organic light-emitting diodes, *J. Mater. Chem.* **21**, 19187 (2011).
- [25] T.-A. Lin, T. Chatterjee, W.-L. Tsai, W.-K. Lee, M.-J. Wu, M. Jiao, K.-C. Pan, C.-L. Yi, C.-L. Chung, K.-T. Wong, and C.-C. Wu, Sky-blue organic light emitting diode with 37% external quantum efficiency using thermally activated delayed fluorescence from spiroacridine-triazine hybrid, *Adv. Mater.* **28**, 6976 (2016).
- [26] K.-H. Kim and J.-J. Kim, Origin and control of orientation of phosphorescent and TADF dyes for high-efficiency OLEDs, *Adv. Mater.* **30**, 1705600 (2018).
- [27] D. Yokoyama, A. Sakaguchi, M. Suzuki, and C. Adachi, Horizontal orientation of linear-shaped organic molecules having bulky substituents in neat and doped vacuum-deposited amorphous films, *Org. Electron.* **10**, 127 (2009).
- [28] M. Flämmich, D. Michaelis, and N. Danz, Accessing OLED emitter properties by radiation pattern analyses, *Org. Electron.* **12**, 83 (2011).
- [29] L. Penninck, F. Steinbacher, R. Krause, and K. Neyts, Determining emissive dipole orientation in organic light emitting devices by decay time measurement, *Org. Electron.* **13**, 3079 (2012).
- [30] I. J. Ko, H. Lee, J. H. Park, G. W. Kim, R. Lampande, R. Pode, and J. H. Kwon, An accurate measurement of the dipole orientation in various organic semiconductor films using photoluminescence exciton decay analysis, *Phys. Chem. Chem. Phys.* **21**, 7083 (2019).
- [31] J. Frischeisen, D. Yokoyama, A. Endo, C. Adachi, and W. Brütting, Increased light outcoupling efficiency in dye-doped small molecule organic light-emitting diodes with horizontally oriented emitters, *Org. Electron.* **12**, 809 (2011).
- [32] M. J. Jurow, T. Lampe, E. Penzo, J. Kang, M. A. Koc, T. Zechel, Z. Nett, M. Brady, L.-W. Wang, A. P. Alivisatos, S. Cabrini, W. Brütting, and Y. Liu, Tunable anisotropic photon emission from self-organized CsPbBr₃ perovskite nanocrystals, *Nano Lett.* **17**, 4534 (2017).
- [33] T. Morgenstern, M. Schmid, A. Hofmann, M. Bierling, L. Jäger, and W. Brütting, Correlating optical and electrical dipole moments to pinpoint phosphorescent dye alignment in organic light-emitting diodes, *ACS Appl. Mater. Interfaces* **10**, 31541 (2018).
- [34] L. Penninck, P. D. Visschere, J. Beeckman, and K. Neyts, Dipole radiation within one-dimensional anisotropic microcavities: A simulation method, *Opt. Express* **19**, 18558 (2011).
- [35] C.-K. Moon, S.-Y. Kim, J.-H. Lee, and J.-J. Kim, Luminescence from oriented emitting dipoles in a birefringent medium, *Opt. Express* **23**, A279 (2015).
- [36] N. Danz, N. Haase, A. Morherr, C. Pflumm, B. Fritsch, and D. Michaelis, in *Organic Electronics and Photonics: Fundamentals and Devices* (International Society for Optics and Photonics, Strasbourg, 2018), Vol. 10687.
- [37] M. Flämmich, M. C. Gather, N. Danz, D. Michaelis, A. H. Bräuer, K. Meerholz, and A. Tünnermann, Orientation of emissive dipoles in OLEDs: Quantitative *in situ* analysis, *Org. Electron.* **11**, 1039 (2010).